

# Gap Formation by Planets in Turbulent Protostellar Disks

Wayne F. Winters<sup>1</sup>, Steven A. Balbus<sup>1</sup>, and John F. Hawley<sup>1</sup>

## ABSTRACT

The processes of planet formation and migration depend intimately on the interaction between planetesimals and the gaseous disks in which they form. The formation of gaps in the disk can severely limit the mass of the planet and its migration toward the protostar. We investigate the process of gap formation through magnetohydrodynamic simulations in which internal stress arises self-consistently from turbulence generated by the magnetorotational instability. The simulations investigate three different planetary masses and two disk temperatures to bracket the tidal (thermal) and viscous gap opening conditions. The results are in general qualitative agreement with previous simulations of gap formation, but show significant differences. In the presence of MHD turbulence, the gaps produced are shallower and asymmetrically wider than those produced with pure hydrodynamics. The rate of gap formation is also slowed, with accretion occurring across the developing gap. Viscous hydrodynamics does not adequately describe the evolution, however, because planets capable of producing gaps also may be capable of affecting the level MHD turbulence in different regions of the disk.

*Subject headings:* protostellar disks — planet formation — MHD — instabilities

## 1. Introduction

Understanding the process of planet formation in nascent solar systems is a long-standing goal of astrophysical theory. The traditional picture is an orderly one in which planets slowly build up their mass first by accreting rocky planetesimals, then (if sufficiently massive) gas from the surrounding protostellar disk. The recent multiple detections of extra-solar planets close to the central star, a configuration once thought to be highly improbable, pose a stern challenge to this relatively simple picture of planet formation. In the wake of

---

<sup>1</sup>Dept. of Astronomy, University of Virginia, PO Box 3818, Charlottesville, VA 22903, USA. jh8h@virginia.edu; sb@virginia.edu

these discoveries, contemporary theories emphasize the importance of the dynamical interaction between a developing planet and the ambient gaseous disk.

A possible explanation for the presence of giant planets near their central star is that they have migrated inwards after having formed farther out in the disk. This requires angular momentum to be removed from the planet by an imbalance in the positive and negative torques exerted upon it (Goldreich & Tremaine 1980; Ward 1986, 1997). Two mechanisms have been identified, known as Type I and Type II migration. Type I migration is essentially a linear process in which the planet excites trailing density waves at the Lindblad resonances. The waves carry angular momentum outward through the disk. There are torques of opposite signs exerted at both the inner and outer resonances, but for a given  $m$  (azimuthal wavenumber), the outer resonance lies closer to the planet and the coupling is stronger (Ward 1997). Therefore, if the interaction is dominated by the Lindblad torques, then more angular momentum is lost than acquired by the planet, which would then drift inward. The role of corotation torques, however, is still under investigation, and needs to be understood if Type I migration is to be put on a firm theoretical footing (Tanaka, Takeuchi, & Ward 2002). In Type II migration, nonlinear gravitational interactions between the disk and the planet clear a gap at the orbital radius of the planet (Lin & Papaloizou 1979, 1993; Goldreich & Tremaine 1980). Disk material then no longer accretes across the planet's orbital radius, and the planet is carried inward with the disk itself on an accretion time scale. The rate of migration thus depends on whether a gap forms or not, and whether there is, in fact, an turbulent stress to drive accretion in the disk. Unless for some reason disk material remains abundant in the immediate vicinity of the planet, one important consequence of gap formation is likely to be that planet formation will be severely limited.

Traditionally, turbulence has been modeled as a Stokesian viscosity in accretion disk studies, and the criteria for a planet to open a gap are not the same in viscous and inviscid models. Lin & Papaloizou (1993) and Bryden et al. (1999) discuss the conditions pertinent to each class of model. In the case of an inviscid accretion disk, the competing forces are the local fluid pressure, which resists the creation of a gap, and the planet's gravitational tidal force, which promotes gap formation. The tidal criterion for gap formation is that a gap can form if the planet's Roche (or Hill) radius  $R_R$  exceeds the pressure scale height  $H$ , which we define as the ratio of isothermal sound  $c_s$  to local orbital frequency  $\Omega$ . For a planet of mass  $M_p$  orbiting a central star of mass  $M_*$  at radius  $R_p$ , the Roche limit is  $R_R = (M_p/3M_*)^{1/3}R_p$ . Thus a gap forms if

$$q \equiv \frac{M_p}{M_*} \gtrsim 3 \left( \frac{H}{R_p} \right)^3. \quad (1)$$

Denoting the right hand side of equation (1) as  $q_t$ , the tidal criterion is simply  $q \gtrsim q_t$ .

In viscous disk models, there is another condition that must be satisfied before a gap can open. This is set by the requirement that the rate at which planetary torques clear the gap must exceed the rate at which viscous torques replenish it. The condition is (Lin & Papaloizou 1993)

$$q \gtrsim q_v \equiv 40\alpha \left( \frac{H}{R_p} \right)^2, \quad (2)$$

where  $\alpha$  is defined as the ratio of the viscosity to  $c_s H$ . This is essentially the Shakura & Sunyaev (1973) parameterization

These gap conditions have been extensively investigated via two-dimensional numerical simulations of  $\alpha$  disks (Bryden et al. 1999; Kley 1999; Lubow, Seibert, & Artymowicz 1999). An important limitation of this approach is that the most interesting consequences of the planet-disk interaction depend upon the nature of the stress, and viscosity is not synonymous with turbulence. The origin of the anomalous disk stress and turbulent transport is no longer unapproachable. If  $\alpha$  represents a stress arising from internal disk turbulence, then the source of this turbulence is magnetic (Balbus & Hawley 1991). As discussed by Balbus & Hawley (1998) purely hydrodynamic sources of turbulence are problematic at best, and none has been observed and sustained in a fully three-dimensional simulation of a Keplerian disk. The problem is illustrated by studies of convective turbulence: when this form of turbulence is imposed, it drives inward, not outward, angular momentum transport (Stone & Balbus 1996). This is no fluke of the peculiar properties of convection, it is what happens quite generally if incompressible turbulence is driven in a rotationally stable disk. If nonlinear instabilities were a possibility, they would be present in convective and shearing sheet simulations (Hawley, Balbus, & Winters 1999). The shearing sheet is scale-free and any instabilities would accordingly not require extremely large Reynolds numbers to appear. (There is nothing special about the behavior of very small scale disturbances that would not also be seen at larger scales.) This is why Hawley, Balbus, & Winters (1999) easily found nonlinear planar Couette flow instabilities. Their absence from any numerical simulation of a Keplerian disk casts doubt on their existence. Trailing density waves transport angular momentum outwards of course, but their excitation and maintenance must be explained, and this is most readily done only if the disk itself is strongly self-gravitating. Even in this case, the transport properties are generally nonlocal, and not well-suited to an  $\alpha$  formalism description (Balbus & Papaloizou 1999). The nature of, and difficulties with, an  $\alpha$  disk associated with direct planetary torques have recently been discussed by Goodman & Rafikov (2001) (see also Lin & Papaloizou (1996)).

In this paper we perform numerical experiments of planets in protostellar disks in which the internal turbulence and its stress arise self-consistently from the magnetorotational instability. These simulations examine how turbulence affects the formation of gaps in the

disk, and, equally importantly, how the planet affects the turbulence. In this first study we will assume ideal MHD, and not address the issue of the ionization state of the disk, or the degree of magnetically coupling in the gas. These issues are far from resolved (Fromang, Terquem, & Balbus 2002). It is of interest to examine the “simplest” case first.

The plan of this paper is as follows: in §2 we describe the numerical model used for the simulations. In §3 we present several two dimensional hydrodynamic simulations. These models serve as code tests, they provide a comparison with previous numerical work, and they are the controls for the MHD simulations which follow in §4. We present our conclusions in §5.

## 2. Numerical Model

The governing equations for the evolution of a magnetized gaseous disk in the ideal MHD limit are the equation of continuity,

$$\frac{\partial \rho}{\partial t} + \nabla \cdot (\rho \mathbf{v}) = 0, \quad (3)$$

the equation of motion,

$$\rho \frac{\partial \mathbf{v}}{\partial t} + (\rho \mathbf{v} \cdot \nabla) \mathbf{v} = -\nabla \left( P + \frac{B^2}{8\pi} \right) - \rho \nabla \Phi + \left( \frac{\mathbf{B}}{4\pi} \cdot \nabla \right) \mathbf{B}, \quad (4)$$

and the induction equation

$$\frac{\partial \mathbf{B}}{\partial t} = \nabla \times (\mathbf{v} \times \mathbf{B}). \quad (5)$$

In these equations  $\rho$  is the disk mass density,  $\mathbf{v}$  is the fluid velocity,  $P$  is the pressure,  $\mathbf{B}$  is the magnetic field vector, and  $\Phi$  is the gravitational potential. These equations are solved in a cylindrical coordinate system,  $(R, \phi, z)$ , in the “cylindrical disk” limit, in which vertical gravitational forces are ignored. Time and length units are fixed by setting  $GM_* = 1$ , which makes the Keplerian angular velocity,  $\Omega [= (GM_*/R^3)^{1/2}] = 1$  at  $R = 1$ .

The equation of state is “locally isothermal,” with a prescribed temperature profile,  $T(R) \propto R^{-1}$ . This is the same equation of state used in many of the previous planet-disk simulations, e.g., Kley (1999); Bryden et al. (1999); Nelson et al. (2000). Specifically,

$$P = \rho c_s^2 = \rho \left( \frac{H}{R} \right)^2 \frac{GM_*}{R}, \quad (6)$$

where  $H/R$  is a fixed input parameter of a given simulation. In this model, the Mach number of the flow ( $v_\phi/c_s$ ) is constant with radius. The initial disk is given a density profile  $\rho \propto R$

with  $\rho = 1$  at  $R = 1$ . This ensures that the initial pressure gradient is zero. The equations that are explicitly integrated also contain an artificial viscosity of the form described by Stone & Norman (1992a). This is nonzero only in regions of local compression and acts only on the momentum, since the temperature at any given radius is fixed. Its principal function is to spread shock transitions over a few grid zones.

The computational grid consists of a cylindrical annulus centered on the central star, with the radial coordinate running between  $0.25 < R < 3.75$ . The use of an annulus avoids the singularity associated with  $R = 0$ . The angle  $\phi$  runs over the full range from 0 to  $2\pi$ . The vertical grid size,  $L_z$ , is set equal to twice the scale height  $H$  at the radius of the planet,  $R_p$ , i.e., for  $H/R = 0.05$ ,  $L_z = 0.2$ . The three dimensional grid resolution is  $128 \times 128 \times 32$  in  $(R, \phi, z)$ . We work in the ideal MHD limit of a single, infinitely conducting medium.

The gravitational potential for the central star is  $\Phi = -GM_*/R$ . The planet is assumed to remain on a fixed circular orbit with a fixed orbital velocity at radius  $R_p = 2$ . The planet's orbital frequency is

$$\Omega_p^2 = \frac{G}{R_p^3}(M_* + M_p), \quad (7)$$

and the planet's angular location  $\phi_p$ , is a function of time,

$$\phi_p = \phi_0 + \Omega_p t. \quad (8)$$

The gravitational potential of the planet is that of a softened point particle, specifically,

$$\Phi_p = -GM_p/(d^2 + b^2)^{1/2}, \quad (9)$$

where  $d$  is the distance from the planet to a location within the grid,  $d^2 = R^2 + R_p^2 - 2RR_p \cos(\phi - \phi_p)$ , and  $b$  is the softening parameter set to be a fraction of the size of the planet's Roche radius. In the simulations below,  $b$  was set to be equal to one-fifth of the size of the Roche radius for a planet with  $q = 0.001$ , corresponding to  $b = 0.0277$ . The radial and angular gravitational force per unit volume from a planet at a point  $(R, \phi)$  are

$$f_R = -\rho GM_p \left[ \frac{(R - R_p \cos(\phi - \phi_p))}{(R^2 + R_p^2 - 2RR_p \cos(\phi - \phi_p) + b^2)^{3/2}} - \frac{\cos(\phi - \phi_p)}{R_p^2} \right] \quad (10)$$

$$f_\phi = -\rho GM_p \left[ \frac{(R_p \sin(\phi - \phi_p))}{(R^2 + R_p^2 - 2RR_p \cos(\phi - \phi_p) + b^2)^{3/2}} + \frac{\sin(\phi - \phi_p)}{R_p^2} \right]. \quad (11)$$

Since the origin of the coordinate system is non-inertial, the potential includes the indirect term (which accounts for the acceleration of the computational frame). Note that the planet is represented only as a potential; there is no mass loss from the grid at its location, and we do not attempt to model accretion onto the planet in detail.

We have run two types of simulation: inviscid hydrodynamic models in two dimensions  $(R, \phi)$ , and three-dimensional turbulent MHD simulations. Because neither the MRI nor field amplification can operate without vertical structure, simulations of MRI-induced turbulence must be three-dimensional. However, some simplification is still required to make the problem tractable. The cylindrical disk approximation makes it practical to compute disks that have small  $H/R$  values without the need for an unduly large number of grid zones. This cylindrical limit was previously employed by Hawley (2001) in simulations of MHD turbulence in cold Keplerian disks.

For the MHD simulations the initial magnetic field strength is set by the input parameter,

$$\beta = 8\pi P/B^2, \quad (12)$$

which specifies the ratio of the gas pressure to the magnetic pressure. To minimize difficulties with the magnetic radial boundaries, the initial magnetic field is confined to the region between  $R = 0.45$  and  $R = 3.55$ . The subsequent evolution does allow field to leave through the radial boundaries, however.

The equations were solved using time-explicit Eulerian finite differencing. The numerical algorithm is that used by the ZEUS code for hydrodynamics (Stone & Norman 1992a) and MHD (Stone & Norman 1992b; Hawley & Stone 1995). The imposed boundary conditions are periodic along the azimuthal and vertical directions. The radial boundary conditions are somewhat more complex and are set in ghost zones exterior to the inner and outer radial limits of the disk. The density  $\rho$  in the ghost zones is held fixed in time at its initial value. The azimuthal velocity  $v_\phi$  in the ghost zones is held constant and equal to the appropriate Keplerian value. Both the  $v_r$  and  $v_z$  velocity components in the ghost zones are set equal to the last physical values computed at the adjacent boundary. In the 3D MHD cases, the magnetic ghost radial boundaries are that  $B_\phi$  and  $B_z$  vanish, and  $B_r$  is set so that it is divergence-free in the ghost zones. Although straightforward to implement, these boundary conditions are at least partially reflecting, and therefore less than ideal.

The simulations produce a significant amount of both spatial and temporal data. To facilitate the analysis, two-dimensional data were averaged azimuthally, and three-dimensional quantities were averaged both vertically and azimuthally. The definition for the average of some quantity  $X$  is

$$\langle X \rangle = \frac{\int X R d\phi dz}{\int R d\phi dz}. \quad (13)$$

These averages were computed at regular time intervals for each radial grid zone, and the results used to construct space-time diagrams that characterize the overall evolution.

Table 1: Hydrodynamic Simulations

Label	$q$	$H/R$	$q/q_t$	$\tau_{\text{gap}}$
HSP	$2 \times 10^{-4}$	0.05	0.52	530 orbits
HMP	$1 \times 10^{-3}$	0.05	2.6	90 orbits
HLP	$5 \times 10^{-3}$	0.05	13.0	40 orbits
HMPH	$1 \times 10^{-3}$	0.09	0.45	310 orbits
HSPC	$2 \times 10^{-4}$	0.02	8.3	140 orbits

### 3. Hydrodynamic Tests

We begin with a series of purely hydrodynamic simulations to test the numerical model and to establish a baseline for comparison with the results from MHD simulations. Two-dimensional ( $R, \phi$ ) hydrodynamic simulations have been carried out by a number of other researchers, e.g, Bryden et al. (1999); Lubow, Seibert, & Artymowicz (1999); Kley (1999); Nelson et al. (2000). Kley, D’Angelo, & Henning (2001) performed three-dimensional simulations and found that their results largely agree with those from two dimensional simulations so long as the scale height of the disk is comparable to or less than the Roche radius  $R_R$  of the planet, which is the tidal condition for gap formation. For  $H > R_R$  the accretion rate onto the planet can differ between two and three dimensional studies.

The disk temperature profile is set by the selected scale height ratio. The standard value,  $H/R = 0.05$ , corresponds to a constant Mach number of 20 throughout the disk. The initial components of the velocity are  $v_r = 0$  and  $v_\phi = (GM_*/R)^{1/2}$ . Three different planet masses are used, with mass ratios  $q = 2 \times 10^{-4}$ , to  $1 \times 10^{-3}$ , and  $5 \times 10^{-3}$ . Other parameters for the simulations may be found in Table 1. The three main simulations are labeled HSP, HMP, HLP for Hydrodynamic Small, Medium, and Large mass Planet respectively. The ratio of  $q$  to the tidal limit  $q_t$  (eqn. 1) is given for each problem. For  $H/R = 0.05$  the small mass planet has  $q < q_t$ , the medium mass is exceeds  $q_t$ , and the large mass amply satisfies the tidal criterion. For the HMPH(ot) simulation the temperature is increased sufficiently that the medium mass planet no longer meets the tidal condition for gap formation. In the HSPC(old) simulation the temperature is reduced so that the small mass planet can satisfy the tidal condition. Thus the ensemble of simulations bracket  $q_t$  both through different planet masses and different values of  $H/R$ .

Figure 1 shows the distribution of density after 100 planetary orbits for the three simulations with the same  $H/R$ . A qualitative comparison of these plots illustrates how the width of the gap produced changes with the mass ratio: HSP fails to produce a gap, while

See f1.jpg

Fig. 1.— Log density in hydrodynamic simulations after 100 planet orbits for (a) the small mass planet,  $q = 2 \times 10^{-4}$ , (b) the medium mass planet,  $q = 1 \times 10^{-3}$ , and (c) the large mass planet,  $q = 5 \times 10^{-3}$ . The color map runs from blue to red in  $\log(\rho)$  from  $\rho = 0.01$  to 1.0. Note the density enhancements inside the gap at the trailing and leading Lagrange points, L4 and L5.

HLP produces an extensive one. Although the small mass planet does not create a gap, the density is nevertheless reduced within a region near its orbit. In the HSP run the reduced density region is spanned by approximately 10 radial grid zones while the gaps in the HMP and HLP runs are spanned by 30 and 45 radial grid zones, respectively. Also visible are the spiral density waves that the planets generate. The amplitude of these waves increases with planetary mass. Note too the density enhancements at the trailing and leading Lagrange points, L4 and L5, particularly in the HMP run.

The density contours immediately surrounding the planet appear elongated. This is an artifact arising from the aspect ratio of the  $R$  and  $\phi$  grid at the radius of the planet. The grid is uniformly spaced in both  $R$  and  $\phi$  and (at the resolution used)  $Rd\phi > dR$  at the planet's orbital radius. The zones are long thin rectangles, and this results in an elongated planet shape. To verify this, a test calculation was run with the number of angular zones increased by a factor of 3.5 giving  $R_p d\phi = dR$  at the planet's radius. With this grid, the resulting density contours around planet are symmetric. Ideally, one would prefer to have square zones at all radii. This would be particularly important in investigating the accretion of material onto the planet. The best approach might be a nested grid around the planet (Lubow, Seibert, & Artymowicz 1999; Ciecielag, Plewa, & Różyczka 2000; D'Angelo et al 2002). In the present experiments, however, we are primarily concerned with the radial structure in the disk, not the accretion onto the planet. The grid we use is a compromise between radial resolution and a practical amount of computational time.

The top panel of Figure 2 shows the radial density profile (normalized by the initial profile) after 120 orbits for runs HSP, HMP, and HLP. In both the middle and high mass cases a gap forms. The bottom panel of Figure 2 shows the time history of the density evolution at the radial location of the planet. The slope of the line is a measure of the rate of gap clearing; not surprisingly this is a function of planet mass. The clearing rate may be characterized by  $\tau_{\text{gap}}$ , defined as the amount of time required for the density at the planet's radius to decrease by a factor of 10. The value of  $\tau_{\text{gap}}$  is obtained by fitting the density versus time at the planet's radius with a function of the form  $\rho/\rho_o \sim 10^{-t/\tau_{\text{gap}}}$ , where  $t$  is the orbital time. The value of  $\tau_{\text{gap}}$  is listed in Table 1.

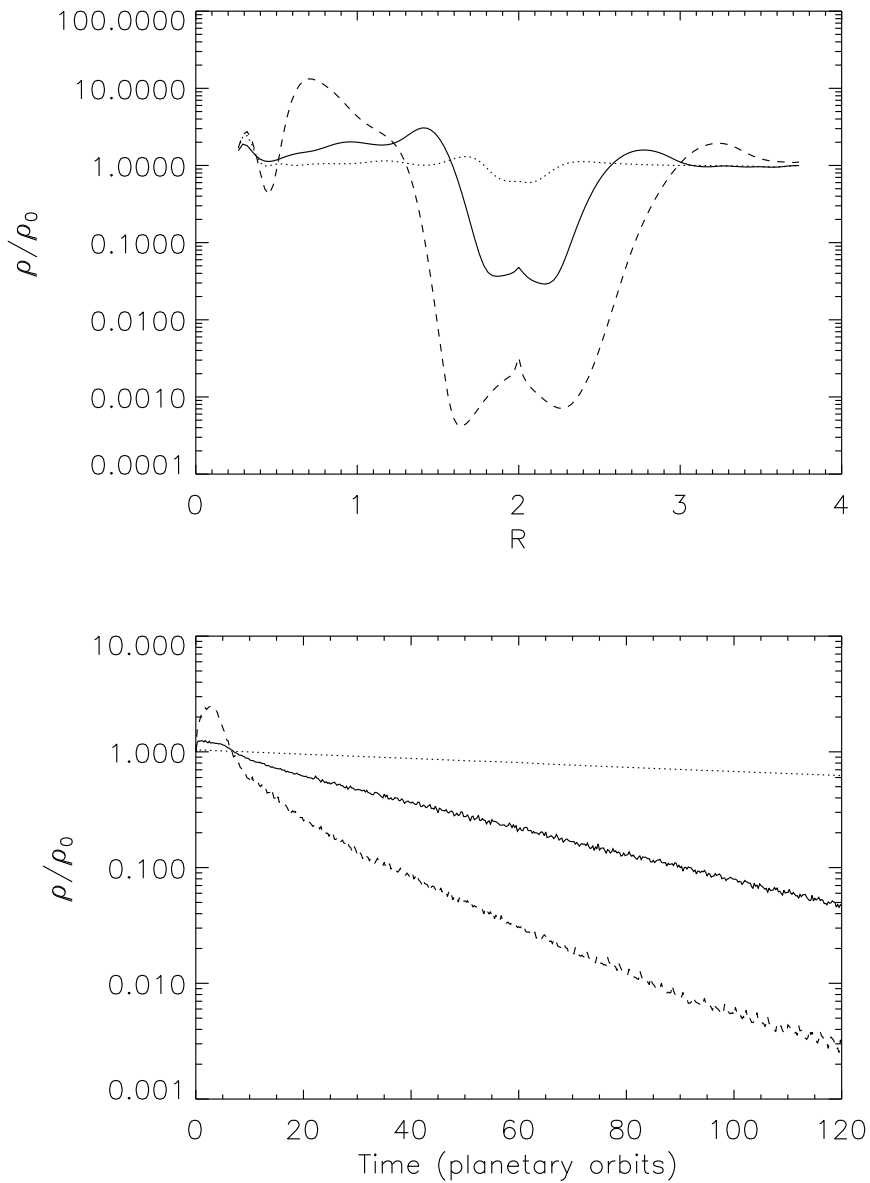


Fig. 2.— Time evolution of the gap density for hydrodynamic (a) The azimuthally-averaged radial density profiles after 120ed line. (b) The time evolution of the azimuthally-averaged density at the planet's orbital radius for each of the three simulations.

The three simulations above test the effect of varying the planet mass, and two further hydrodynamical simulations test the tidal condition with varying disk temperature. In run HMPH the middle mass planet was embedded in a disk that was too hot for it to produce a gap, and in run HSPC the small mass planet was placed in a disk that was cool enough to produce a gap. Figure 3 is the density profile and time-evolution for these two runs. Comparing this data to Figure 2 one can see that cooling the disk increases the rate at which the small mass planet clears its Roche radius, reducing  $\tau_{\text{gap}}$  to 140 orbits. Heating the disk greatly increases  $\tau_{\text{gap}}$  for the middle mass planet, and eliminates the sharp gap boundaries in the density distribution.

To summarize, these hydrodynamic simulations are in agreement with the results of previous work and demonstrate the role of the tidal condition in gap formation in stress-free disks. The Roche radius determines the width of the gap formed, and the temperature in the disk determines whether that radius can be efficiently cleared by the planet’s gravity. These disk simulations will serve as the baseline comparisons for the series of disks with stress from MHD turbulence.

## 4. MHD Turbulence and Gap Formation

### 4.1. MHD turbulent disks

To establish a turbulent background flow, we begin with a planet-free MHD simulation. Previous work with cylindrical representations of MHD turbulence (Hawley 2001; Steinacker & Papaloizou 2002; Nelson, & Papaloizou 2002a) provides some guidance for choosing a suitable initial field configuration. An initial vertical magnetic field produces more powerful turbulence than does an initial toroidal field, but also tends to produce a series of evacuated gaps in the disk, even without the presence of a planet. The extent to which this is physical or an artifact of the cylindrical scheme is not yet well-understood. We have therefore elected to work primarily with toroidal fields, though this is likely to underestimate the strength of the turbulence actually present in a magnetized disk.

Our fiducial simulation starts with a uniform toroidal field with  $\beta = 4$ , and is run for 140 orbits at the radius at which the planet will be inserted. The relatively strong toroidal field ensures that the stress will be reasonably large. Turbulence develops promptly and the resulting stresses drive accretion. The component of greatest importance in the stress tensor is the  $R\phi$  component. For simplicity, we shall refer to this component as “the stress.” The Reynolds stress needs to be defined carefully, since the concept of azimuthal velocity fluctuation makes sense only if the mean azimuthal velocity is known. But the latter must,

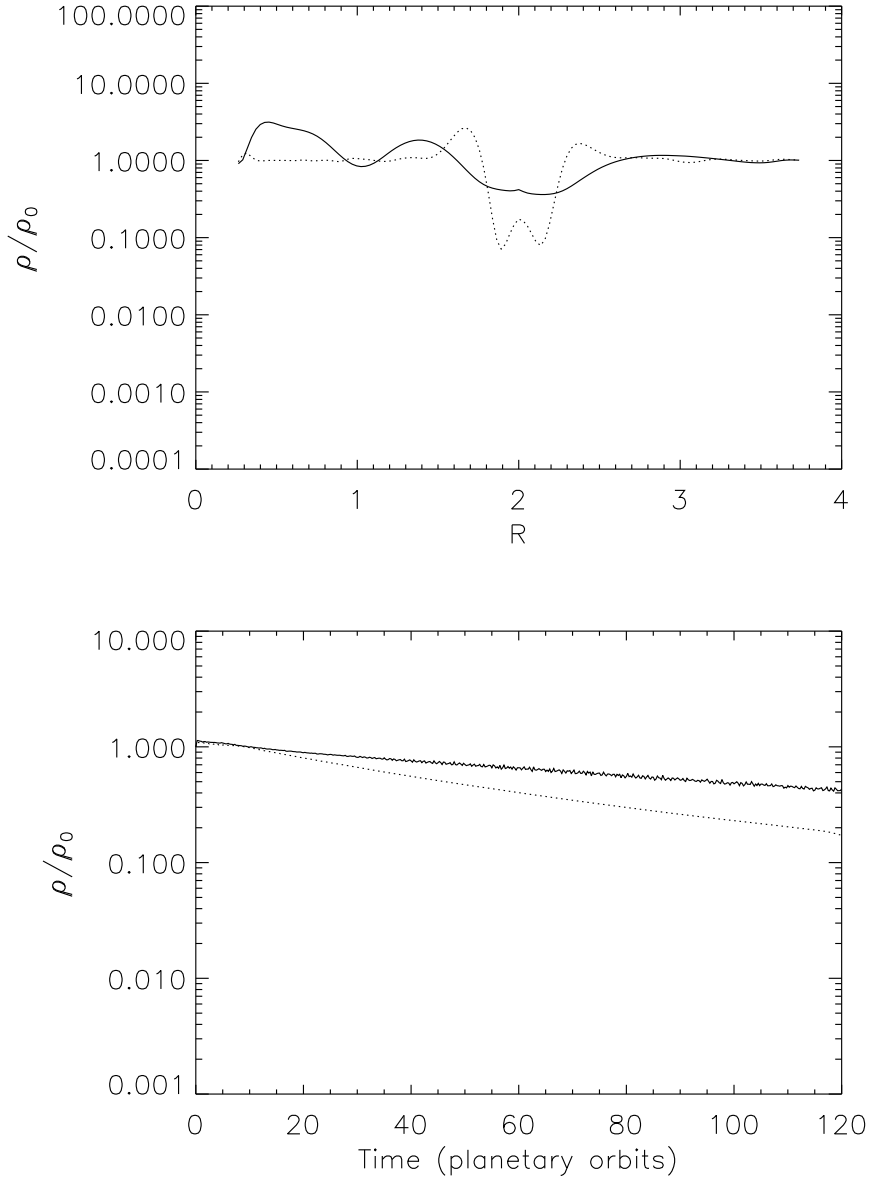


Fig. 3.— Time-evolution of the gap density for hydrodynamic simulations HMPH (solid line) and HSPC (dotted line). (a) The azimuthally-averaged radial density profiles after 120 planetary orbits for each run. (b) The time evolution of the azimuthally-averaged density at the planet's orbital radius for the simulations.

in general, be itself determined from the simulated flow. We follow Hawley (2000), and define the Reynolds stress as

$$\langle \rho v_R \delta v_\phi \rangle = \frac{1}{R} \left( \left\langle \frac{(\rho v_R)(\rho R v_\phi)}{\rho} \right\rangle - \frac{\langle \rho v_R \rangle \langle \rho R v_\phi \rangle}{\langle \rho \rangle} \right). \quad (14)$$

The total turbulent stress is a sum of the Reynolds and  $(R\phi)$  Maxwell stresses.

It is useful to have a dimensionless form for the stress. This, of course, is the role of the classical  $\alpha$  parameter, here defined as

$$\alpha \equiv \frac{1}{P_{\text{initial}}} \langle \rho v_R \delta v_\phi - \frac{B_R B_\phi}{4\pi} \rangle, \quad (15)$$

the stress divided by the initial pressure. The  $\alpha$  parameter is particularly useful for comparisons with the prediction of the viscous gap formation criterion (2), and with the viscous hydrodynamic simulations, e.g., Takeuchi, Miyama, & Lin (1996), Bryden et al. (1999), Kley (1999), and Nelson et al. (2000). The function  $\alpha(R)$  can be obtained by averaging the stress in accordance with equation (13). Figure 4 shows the  $\alpha(R)$  profile at  $t = 40$  orbits for the baseline toroidal field simulation. The Maxwell and Reynolds stresses are also plotted separately. The Maxwell stress is clearly dominant, consistent with earlier studies of MRI-driven accretion disk turbulence (Hawley, Balbus, & Winters 1999). The diminishing of  $\alpha$  at the radial edges is almost certainly a consequence of the initial and boundary conditions, and the true radial dependence (assuming there is one) of  $\alpha$  cannot be determined with certainty. One can, however, extract a reasonable global average, which is  $\alpha = 0.02$ . The magnitude scale of  $\alpha$ , its fluctuation amplitudes, and its general radial variation are all similar to those found in other toroidal field cylindrical disk studies (Hawley 2001; Steinacker & Papaloizou 2002). Translating the globally averaged  $\alpha$  into an effective viscosity and using it in the viscous condition (2) for gap formation, one would conclude that only the large mass planet ( $q = 5 \times 10^{-3}$ ) should be able to clear a gap.

The initial condition for the planet simulations corresponds to orbit 40 of the unforced toroidal field run. For comparison, the unforced run is evolved a further 100 orbits. The top panel of figure 5 shows the radial profile of density normalized by the initial profile at  $t = 40$  (dotted line) and 140 orbits (solid line). The density in the outer disk gradually decreases with time, while the density in the inner disk increases. The density at  $R = 2$ , the radius at which the planet will be inserted, remains nearly constant.

The bottom panel of figure 5 shows the radial profile of the Maxwell stress normalized by the initial pressure. As the simulation evolves, the Maxwell stress in the outer disk decreases. This may be due in part to the reduction in mass and field energy in this region of the disk caused by losses through the outer boundary. As a practical matter, the time over which

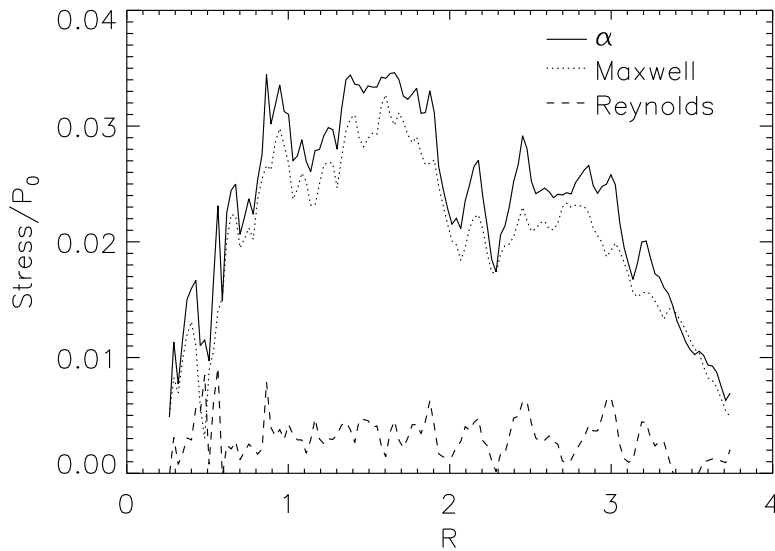


Fig. 4.— Radial profile (solid line) of the vertically and azimuthally averaged turbulent stress  $\alpha$  at  $t = 40$  planetary orbits. The values are scaled in terms of the initial pressure  $P_0$ . Plotted separately are the two components of  $\alpha$ : the dotted line is the Maxwell stress,  $= -B_R B_\phi / 4\pi$ , and the dashed line the Reynolds stress. Throughout the disk the Maxwell stress is dominant.

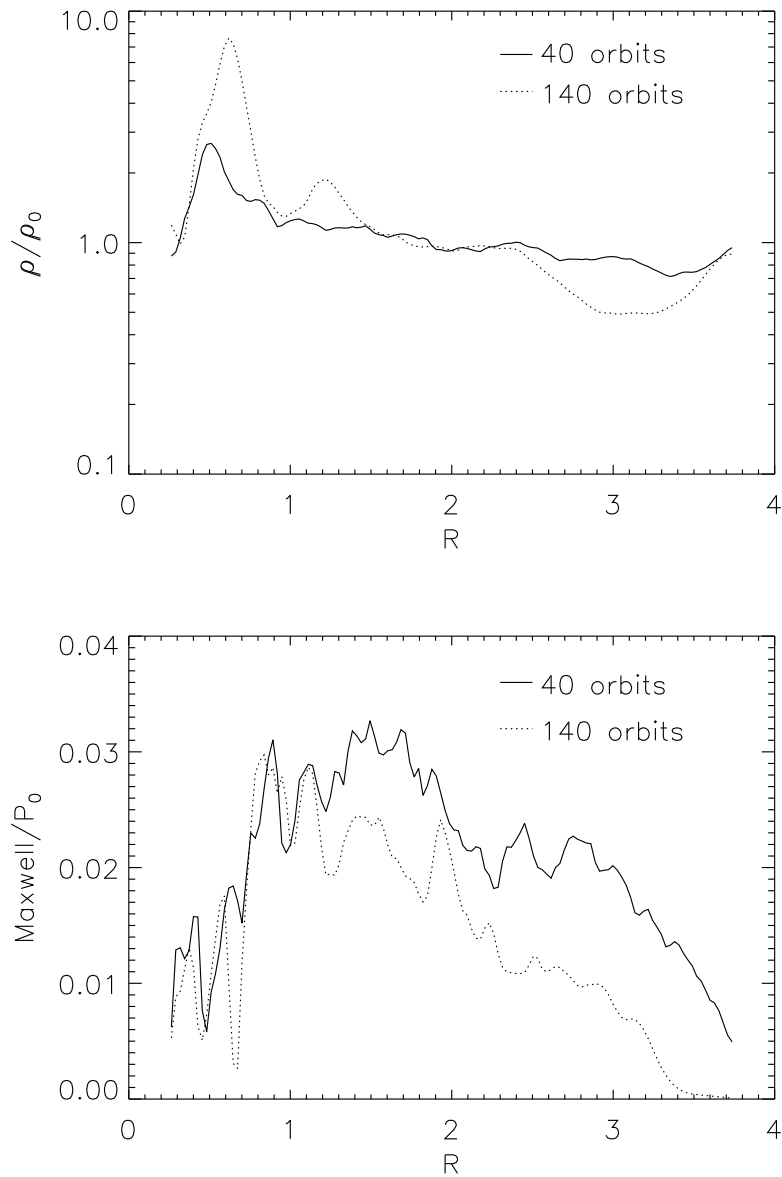


Fig. 5.— Radial profiles of (a) density and (b) Maxwell stress at  $t = 40$  orbits (dotted line) and  $t = 140$  orbits (solid line) in the planetless toroidal field simulation MNP. The change in the radial density profile is due to the presence of substantial accretion driven by the turbulent stresses.

the simulation can be evolved is limited to  $\sim 200$  orbits, by which point significant global evolutionary changes occur.

While the toroidal field model appears to be best suited to the present study, it is desirable to investigate other magnetic geometries, such as a vertical field. But vertical magnetic fields have proven to be so vigorously unstable (Hawley 2001; Steinacker & Papaloizou 2002), that large  $\alpha$  values and substantial evolution occur over a relatively short time interval. In a cylindrical disk, an initial uniform vertical field can only be lost through the boundary, and is otherwise always present to drive the linear “channel mode” of the MRI (Hawley & Balbus 1992). Vertical fields also tend to open up gaps in cylindrical disks even without a planet present: the Maxwell stress increases where the density decreases, and underdense regions become yet more underdense.

One way around these difficulties is to choose an initial magnetic field strength that is so small that the fastest growing unstable wavelength is unresolved. The field strength is set so that fastest growing wavelength,  $\lambda_{max}$ , is set equal to the vertical size of one grid zone,  $\Delta z$ , i.e. (Balbus & Hawley 1998),

$$B_z(R) = (15/16)^{1/2} \Omega(R) (4\pi\rho)^{1/2} \frac{\Delta z}{2\pi}. \quad (16)$$

This constraint artificially “cripples” the MRI, reducing the linear growth rate of the resolved wavelengths, and allowing long duration simulations. The linear growth rate is proportional to  $\sim v_A/N \propto \Omega/N$ , where  $v_A$  is the Alfvén speed, and  $N$  is the number of grid zones of the resolved unstable mode. In the outer portion of the disk this becomes very low. Even with this crippled field, however, there is still some tendency to produce underdense gaps. The unforced simulation develops radially-alternating high and low density regions throughout the disk by orbit 140. The crippled vertical field model should be regarded not so much as a good model for a disk (it is, after all, intentionally underresolved), but as a numerical experiment that provides an alternative turbulent state for comparison with the toroidal field results.

## 4.2. Planets in turbulent disks

The parameters for the MHD simulations with a planet are listed in Table 2. The runs are labeled M for MHD, NP for no planet, or SP, MP, LP for small, medium and large mass planet, and a Z indicates a run with the initial vertical field. Except for the inclusion of magnetic fields, these planet simulations had the same parameters as the hydrodynamic tests described in §3. The value of the viscous gap parameter  $q_v$  used in Table 2 assumes  $\alpha = 0.02$ .

Table 2: 2.5-D MHD Simulations

Label	$q$	$H/R$	$q/q_t$	$q/q_v$	Field Geometry	$\tau_{\text{gap}}$
MNP	0	0.05	–	–	toroidal $\beta = 4$	–
MSP	$2 \times 10^{-4}$	0.05	0.52	0.1	toroidal $\beta = 4$	anti-gap
MMP	$1 \times 10^{-3}$	0.05	2.6	0.5	toroidal $\beta = 4$	215 orbits
MLP	$5 \times 10^{-3}$	0.05	13.0	2.5	toroidal $\beta = 4$	75 orbits
MMPH	$1 \times 10^{-3}$	0.09	0.45	0.17	toroidal $\beta = 12.96$	anti-gap
MSPC	$2 \times 10^{-4}$	0.02	8.3	0.67	toroidal $\beta = 0.64$	60 orbits
MZNP	0	0.05	–	–	Vertical, $\lambda_{\text{max}} = \Delta z$	–
MZMP	$1 \times 10^{-3}$	0.05	2.6	0.5	Vertical $\lambda_{\text{max}} = \Delta z$	90 orbits

Figure 6 shows the density after 100 planetary orbits for runs MSP, MMP, and MLP, and figure 8 is the radial distribution of the Maxwell stress at late time for these simulations. Figure 8 illustrates that the level of turbulent stress is not independent of the planet; this has consequences. One such consequence is illustrated by MSP, a small mass planet that fails to satisfy either the tidal or the viscous gap opening condition. In MSP the density *increases* within the Roche radius of the planet, forming an “anti-gap.” The Maxwell stress has decreased near the planet and gas accretes into this region faster than it leaves. This density rise further decreases the local Alfvén velocity of the fluid, reducing the wavelength of the fastest growing MRI mode, further reducing the stress. Outside of the planet’s Roche radius the low mass planet produces a weak spiral wave, but otherwise has a minimal effect on the evolution of the accretion disk.

See f6.jpg

Fig. 6.— Log density in toroidal field MHD simulations at  $t = 100$  orbits. Plotted are (a) the small mass planet,  $q = 2 \times 10^{-4}$ , (b) the medium mass planet,  $q = 1 \times 10^{-3}$ , and (c) the large mass planet,  $q = 5 \times 10^{-3}$ . The color map runs from blue to red in  $\log(\rho)$  from  $\rho = 0.01$  to 1.0.

The top panel of figure 7 is a comparison of the radial density profiles for the three embedded planet toroidal MHD simulations, similar to the top panel of figure 2. The corresponding plots for each one of the planetary masses are easy to separate by the depth of the gap produced. The low mass planet simulation produces a density increase at the planet’s radius, while the other planets’ gaps are shallower than those seen in the hydro runs, and their outer edges were not as well-defined. Note that the overall slope in the radial density

profile is consistent with the presence of ongoing accretion. The bottom panel of figure 7 displays the time history of the density, similar to the bottom panel of figure 2. Once again, the three different planetary masses can be separated by the rate at which the density decreases. The small mass planet shows a steady increase in density at the planet’s orbit. In the other two cases, the rate of density decrease is much less than with hydrodynamics alone; accretion hampers gap formation.

The middle mass planet (run MMP) satisfies the tidal condition but not the viscous condition. Exceeding the tidal condition ensures that the planet will exert a significant influence on the the accretion disk whether or not it is ultimately able to clear a gap. As is clear from figure 6 the planet was able to produce a noticeable density reduction around its Roche radius. The planet also creates a strong spiral wave in the disk. Most surprisingly, after about 50 planetary orbits, the magnetic stress inside  $R_p$  decreases to very low levels (see fig. 8). Again, not only does the stress in the disk affect the planet’s ability to form a gap, but, at least in these reduced growth rate simulations, the planet can influence the turbulent stress within the disk.

The large mass planet (run MLP) easily satisfies both gap criteria, and its effect on the disk is the most extreme. A large density gap develops rapidly, although the formation time  $\tau_{\text{gap}}$  is increased over the purely hydrodynamic model. A strong global spiral wave is generated, from the inner to the outer radial boundaries. And, as with run MMP, the planet modifies the disk by lowering the Maxwell stress, here in both the inner and outer disk.

In these three runs the planet was placed into an already turbulent magnetized disk. In the next experiment, we approach the problem from another direction: we add a magnetic field to a purely hydrodynamical disk in which a gap has formed. This new simulation, labeled HMMP, is initialized by adding a  $\beta = 4$  toroidal field to the disk from simulation HMP after 100 planetary orbits. The result is a disk with just the same parameters as in simulation MMP. The ordering of the appearance of turbulence and the appearance of a planet does not matter. In MMP, a shallow gap forms even though the mass ratio  $q$  does not exceed the viscous criterion. Adding a magnetic field to HMP has an immediate effect, and accretion begins to fill in the much deeper gap produced without stress.

In figure 9, the top panel shows the radial density profile at the moment the magnetic field is added to the disk (dotted line), and after 100 orbits of MHD evolution (solid line). The bottom panel depicts the time history of the density at the planet’s radius. The initial hydrodynamic phase exhibits an exponential decrease in density as the gap deepens. However, once the toroidal magnetic field is included and turbulence develops, the density at the planet’s radius begins to increase, returning to about the same level that it had at the end of run MMP. At the end of the simulation the gap has become shallower, wider, and

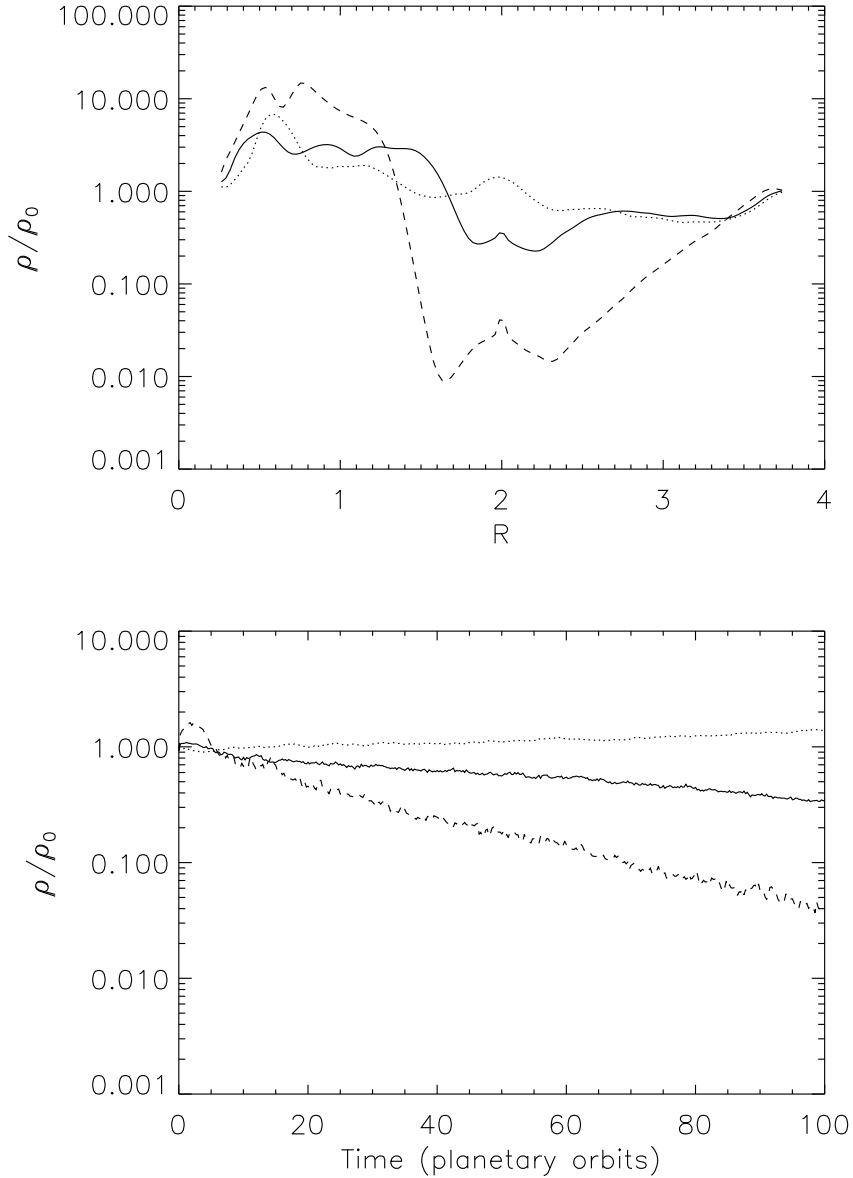


Fig. 7.— Time evolution of the gap density for toroidal MHD simulations MSP (dotted line), MMP (solid line), and MLP (dashed line). (a) The azimuthally-averaged radial density profiles after  $t = 100$  planetary orbits. (b) The time evolution of the azimuthally-averaged density at the planet's orbital radius for each of the three simulations.

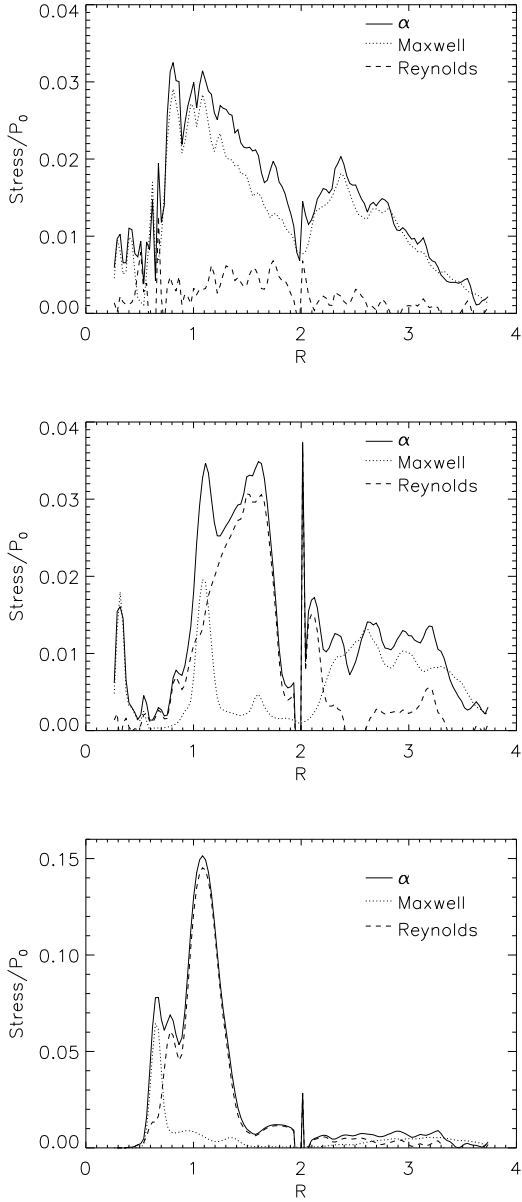


Fig. 8.— Radial profile (solid line) of the vertically and azimuthally averaged turbulent stress  $\alpha$  and the two components of  $\alpha$ : the dotted line is the Maxwell stress,  $= -B_R B_\phi / 4\pi$ , and the dashed line the Reynolds stress. The values are normalized to the initial pressure  $P_0$ . (a) Simulation MSP, the small mass planet. The Maxwell stress remains comparable to the planetless simulation (fig. 4), except in the vicinity of the planet’s orbit. (b) MMP, the medium mass planet. The average Maxwell stress interior to the planet’s orbital radius is significantly reduced where there is a large Reynolds stress from the spiral wave driven by the planet. Overall, total stress  $\alpha$  remains comparable to the planetless simulation. (c) MLP, the large mass planet simulation. The average Maxwell stress interior to the planet’s orbital radius is significantly reduced and the Reynolds stress from the spiral wave is much larger than the total stress in the planetless simulation. The Maxwell stress increases just where the Reynolds stress dies out.

much less well-defined than in the hydrodynamic simulation. The turbulent stresses drive accretion across the gap, increasing the mass in the inner disk at the expense of the outer disk. Apparently a planet that satisfies the tidal criterion, but not the viscous criterion, can form only a partial gap.

We have also examined the effect of varying  $H/R$  by altering the temperature of the underlying disk. To keep the average  $\alpha$  value comparable to the previous simulations, the initial magnetic field strength must also be adjusted. The ratio of the fastest growing wavelength to the disk radius,  $\lambda_{max}/R$ , is held constant by varying  $\beta$ , since

$$\frac{\lambda_{max}}{R} \propto \frac{1}{\sqrt{\beta}} \left( \frac{H}{R} \right). \quad (17)$$

Run MMPH is a hotter disk ( $H/R = 0.09$ ) with the medium mass planet. This planet does not satisfy either the tidal or viscous criterion for gap formation. In fact, an anti-gap, or over-density, is produced, just as in the MSP simulation.

Run MSPEC is a cooler disk with  $H/R = 0.02$ ,  $\beta = 0.64$ , and a small mass planet. It satisfies the tidal criterion, but not the viscous criterion. During the first 60 orbits of evolution, the density drops inside the planet's Roche radius; after that time the rate of decrease declines nearly to zero. The density in the gap levels off at around 8% of its original value, similar to the results of the MMP simulation. When the tidal criterion is satisfied, the density within the Roche radius is reduced, but if the viscous condition is not met, the gap is not completely emptied.

Initially, in run MSPEC there is a measurable Maxwell stress throughout the disk, but once the planet is inserted, the magnetic stress in the inner disk is reduced. A comparison between this simulation and MSP is instructive. When the planet was not able to produce a density gap in MSP, the Maxwell stress was largely unaffected. In the cooler disk, however, the small mass planet did produce a gap, and the turbulence in the inner disk was diminished. This suggests that the threshold for gap production is closely related to the threshold for affecting the disk stress. Evidently, both processes mark the onset of nonlinear disk-planet interactions.

In run MZMP, a medium mass planet in a vertical field, the disk was evolved for 100 orbits, allowing a gap to form. In contrast to run MMP, the Maxwell stress was sustained inside of the planet's orbit, but it is significantly reduced outside of the planet's orbit. Of course even in run MZNP which does not have a planet, it is clear that at large radii in the MHD turbulence is rather weak, so this effect cannot be attributed solely to the presence of the planet. The continued presence of Maxwell stresses in the inner portion of the disk, however, is a significant difference from what is seen in the toroidal field simulation.

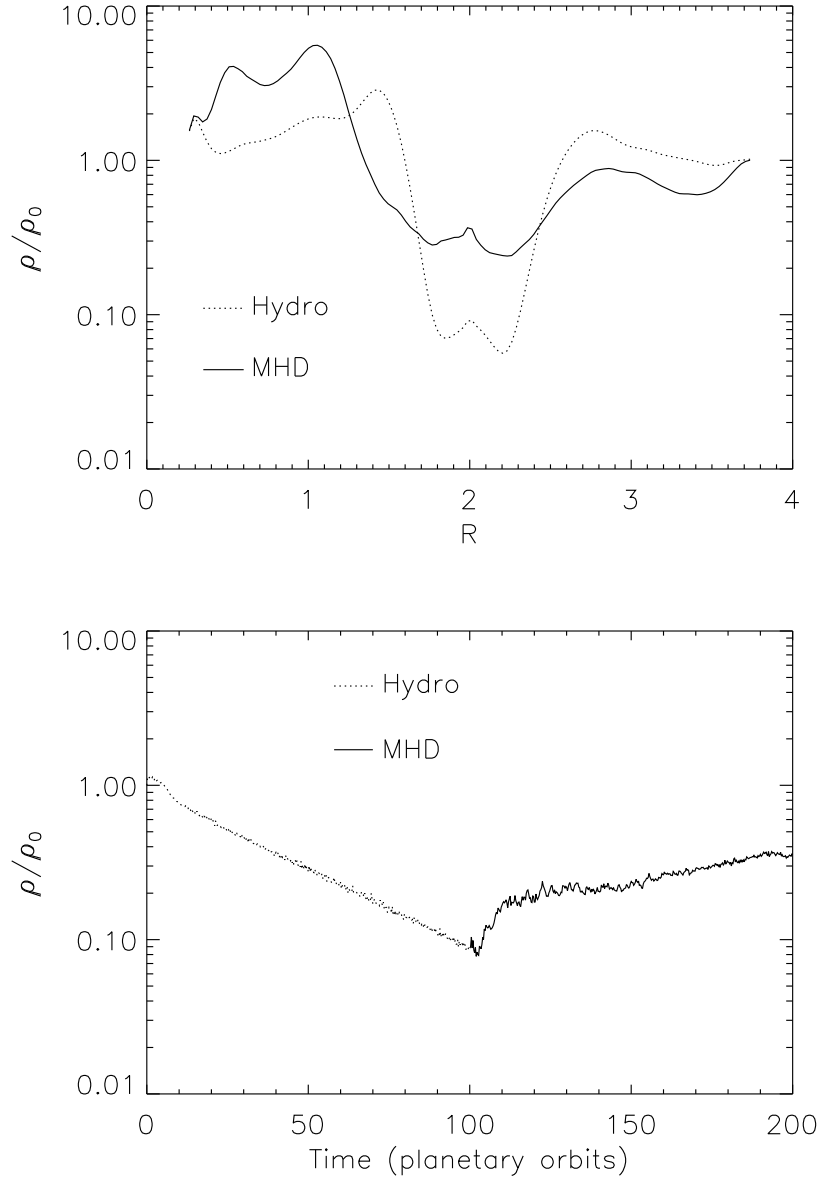


Fig. 9.— Density in simulation HMMP. In this model the first 100 planetary orbits are purely hydrodynamical. A toroidal magnetic field is then added, MHD turbulence develops, accretion into the gap begins, and the gap becomes wider and shallower. (a) Radial density profile at the end of HMMP compared with the density at the end of the purely hydrodynamic portion of the run. (b) Time history of the density at the orbit of the planet.

Comparing the density evolution in run HMP with MZMP we find remarkably good agreement between the two simulations. Even though the turbulent stresses are initially present in the MHD simulation, the resulting density profile and time history are essentially those of the hydro simulation. The reason for this is clear. In the MHD simulation at late times, the Maxwell stress in the outer disk is drastically reduced, effectively ending inward accretion. With no fluid moving from the outer disk to the inner, nothing flows across the gap. Consequently, the rate of gap formation and radial profile of the gap are the same as in the hydro simulation.

### 4.3. Effect of planet on stress

The simulations have provided evidence that not only does the stress affect the formation of a gap around the planet, but, under some circumstances, the planet can directly influence the turbulent stress. In run MSP, the stress was reduced only within the planet’s Roche radius, while in the larger mass planet runs (MMP and MLP), throughout most of the inner disk the Maxwell stress was significantly reduced at late times. This occurs more rapidly with the large mass planet.

The question naturally arises whether the presence of the planet directly causes the reduction of the MHD stress, or whether changes in the disk and magnetic field due to the overall evolution have altered the MRI stability properties of the disk. To distinguish between these possibilities we return to the end of run MMP and remove the planet. The disk, magnetic field, and gap remain, but the spiral wave is quickly lost once the planet is gone.

Figure 10 shows the before and after radial profiles of density (top panel) and Maxwell stress (bottom panel). The solid lines correspond to the point in time when the planet was removed, and the dashed lines are from 20 orbits later. The bottom panel dramatically shows how the Maxwell stress in the inner disk recovers after the removal of the planet, increasing by a factor of 10 after 20 orbits. The density distribution, on the other hand, changes only slightly over this same time. The most noticeable change in the radial density profile is that the gap has become shallower and its edges less defined. This experiment suggests that interactions between the spiral density wave and the MHD turbulence affects the level of the Maxwell stress.

The planet’s influence on the disk as a whole is clearly manifest as a large spiral wave. Figure 11 displays vertically-averaged Maxwell stress images from planetless simulation and the two small-planet MHD simulations, MSP and MSPEC. Without a planet, the magnetic

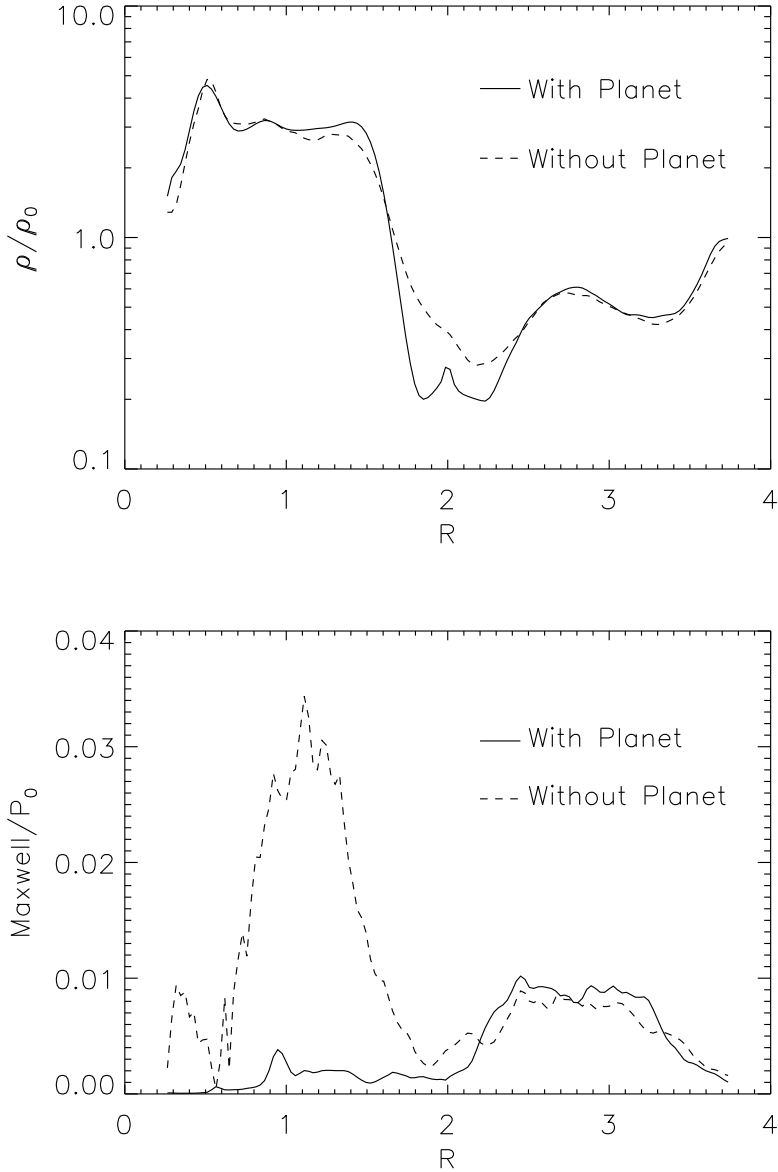


Fig. 10.— (a) Radial density profile, and (b) Radial profile of the Maxwell stress ( $= -B_R B_\phi / 4\pi$ ) at the end of run MMP (solid line), and 20 orbits of subsequent evolution after the planet is removed (dashed line). Once the planet is removed, the Maxwell stress interior to the planet's orbit recovers to its former value as the Reynolds stress due to the spiral wave dies out.

stress is spread evenly throughout the disk. In the MSP run, the planet is not able to form a gap. The planet produces a spiral wave that is strong only near the planet. When the disk is cooled in the MSPEC simulation, the small mass planet is able to form a gap. As can be seen from the bottom image, the planet now has a much more extended influence on the magnetic stress. The inference is that if the planet is massive enough to create a gap, it is massive enough to produce a spiral density wave that interacts with, and lowers, the turbulent Maxwell stress in the disk interior.

See f11.jpg

Fig. 11.— Contours of the late time, vertically averaged Maxwell stress from (a) the planetless simulation, (b) the small mass planet simulation MSP, and (c) the cold small mass planet simulation MSPEC. Values are scaled by the initial pressure  $P_0$ . Negative values are blues and cyans and run from  $-0.1$  to  $0$ . Positive values are yellows and reds and run from  $0$  to  $0.1$ . When the temperature is reduced in MSPEC, the planet’s influence on the rest of the disk becomes stronger and a strong global spiral wave develops. The presence of this strong wave coincides with the local reduction in the Maxwell stress.

It should be noted that this effect may well be sensitive to the choice of a toroidal field. The Maxwell stress in the crippled vertical field run MZMP was not substantially reduced by the planet, even though it did form a gap. This point requires further study.

## 5. Conclusions

In this paper we have examined the formation of gaps by planets in protostellar disks in the presence of Maxwell and Reynolds stresses produced by MHD turbulence. The aims of this first study were to test the tidal and viscous conditions for gap formation, and to observe the effects of the planet on an MHD turbulent disk.

We began with a series of inviscid hydrodynamic simulations as controls. Under these conditions gap formation is determined by the tidal criterion: a planet will clear a gap when the local Roche radius is greater than the pressure scale height. Our hydrodynamic simulations agreed with this condition and with the many simulations of such disks already in the literature.

To establish a turbulent disk, we ran an initial toroidal field configuration for 40 planetary orbits prior to the insertion of the planet itself. The resulting disk had significant Maxwell and Reynolds stresses that vary with radius, but which gave an average  $\alpha$  value of

0.02. A planet was then added, and the results compared with the tidal and with the viscous criteria for gap formation.

When the planet was insufficiently massive, or the disk too hot to satisfy the tidal condition, a gap did not form. In fact, the density around the planet increases. The MHD turbulence drives an overall accretion flow from the outer to the inner disk, and because the planet is able to reduce the turbulent stress within its Roche radius, there is a local buildup in density.

In several simulations, the planet satisfied the tidal criterion, but not the viscous criterion. In this case, the density within the Roche radius is still significantly reduced, but not to zero. The resulting gaps are more shallow than those seen in the pure hydro runs, and the radial density profiles at outer edges of the gap are wider.

When a planet satisfies both the viscous and tidal criteria, a gap formed, but at a reduced rate compared with the hydrodynamic runs. Accretion across the gap continues, and the edges of the gap are somewhat smeared out. The accretion rate is not large enough to prevent the density within the gap from being driven to a very low level.

In a recent paper, Nelson, & Papaloizou (2002b) present a simulation of a planet placed in an MHD turbulent disk. Their simulation considered a  $q = 5 \times 10^3$  mass planet (equivalent to our high mass planet) on a cylindrical grid with a disk model that has the same radial power law dependence on  $\rho$  and  $P$  in the main part of the disk as the model as described in §2. They use  $H/R = 0.1$  (hotter than our models), and an initial sinusoidally-varying vertical field that produces MHD turbulence with an averaged  $\alpha$  value of 0.005 compared with our models that use a stronger toroidal field with  $\alpha \sim 0.02$ . Nelson & Papaloizou ran a single simulation with higher resolution than our models. The focused on the interaction of the planet with a disk and a pre-existing gap, whereas our aim is to consider the gap formation process itself in the presence of MHD turbulence.

Nelson, & Papaloizou (2002b) found, as we did, that spiral waves produced by the planet reduced the stresses provided by the MHD turbulence; they observed this effect mainly near the gap where the waves were strong. They do not observe evidence for accretion across the gap, whereas some of our simulations show this. This suggests that whether or not there is accretion across the gap depends on such parameters as  $q$ ,  $\alpha$ , and  $H/R$ .

Some results do not differ dramatically from those seen in viscous hydrodynamic studies. For example, Kley (1999) found that the tidal condition had a greater effect on the width of the gap and the strength of the spiral waves than variations in viscosity. By determining the rate at which gas flows into the gap, the viscosity affects mainly the accretion rate onto the planet. Nelson, & Papaloizou (2002b) compared their model directly with a viscous model

and found a number of differences in detail. The gap in the turbulent disk model was deeper than the viscous model with equivalent  $\alpha$  value.

Clearly, matters are much more interesting than the viscous models would predict. The presence of the planet itself directly influences the turbulence levels and stress within the disk. This could not be seen with a standard  $\alpha$  viscosity simulation, for in such a model the viscosity can influence, but not be influenced by, the planet. We found that the small mass planet reduced the Maxwell stress in its immediate vicinity, allowing matter to accumulate here. More significantly, the medium and large mass planets were able to reduce the turbulence levels in the disk region interior to their orbits. Tests showed that this was not because the MRI was stabilized by changes within the disk structure. Rather, it appears to be due to a nonlinear interaction between the spiral wave induced by the planet and the turbulence. This wave has to exceed a certain strength to have this effect. In the main part of the disk the rule is when the planet is massive enough to open a gap it can also reduce the turbulent stress. It should be noted that this effect was observed only in the disks where the initial field was toroidal, and not in the simulation with a weak vertical field.

We acknowledge support under NSF grant AST-0070979, and NASA grants NAG5-10655 and NAG5-9266. Some of the simulations described here were carried out on computational platforms supported by the National Center for Supercomputing Applications and the San Diego Supercomputer Center.

## REFERENCES

Balbus, S. A., & Hawley, J. F. 1991, *ApJ*, 376, 214

Balbus, S. A., & Hawley, J. F. 1998, *Rev Mod Phys*, 70, 1

Balbus, S. A., & Papaloizou, J. C. B. 1999, *ApJ*, 521, 650

Bryden G., Chen X., Lin D., Nelson R., & Papaloizou J. 1999, *ApJ*, 514, 344

Ciecielag P., Plewa T., & Różyczka M., 2000, in *Disks, Planetesimals and Planets*, Garzón, C. Eiroa, D. de Winter, and T. J. Mahoney, eds. (San Francisco: ASP) 219, 45

D'Angelo G., Henning T., & Kley W. 2002, *A&A*, 385, 647

Frank, J., King, A., & Raine, D. 1992, *Accretion Power in Astrophysics*, 2nd ed., (Cambridge: Cambridge University Press)

Fromang, S., Terquem, C., & Balbus, S. A. 2002, MNRAS, 329, 18

Goldreich, P., & Tremaine, S. 1980, ApJ, 241, 425

Goodman, J., & Rafikov, R. R. 2001, ApJ, 552, 793

Hawley, J. F. 2000, ApJ, 528, 462

Hawley, J. F. 2001, ApJ, 554, 534

Hawley, J. F., & Balbus, S. A. 1992, ApJ, 400, 595

Hawley, J. F., Balbus, S. A., & Winters, W. F. 1999, ApJ, 518, 394

Hawley, J. F. & Stone, J. M. 1995, Comp Phys Comm, 89, 127

Kley, W. 1999, MNRAS, 303, 696

Kley, W., D'Angelo, G., & Henning, T. 2001, ApJ, 547, 457

Lin, D. N. C., & Papaloizou, J. C. B. 1979, MNRAS, 188, 191

Lin, D. N. C., & Papaloizou, J. C. B. 1993, in Protostars and Planets III, Levy, E., Lunine, J. eds. (Tucson: University of Arizona Press), p. 749

Lin, D. N. C., & Papaloizou, J. C. B. 1996, ARAA, 34, 703

Lubow S., Seibert M., & Artymowicz P. 1999, ApJ., 526, 1001

Nelson, R., & Papaloizou, J. C. B. 2002a, MNRAS, in press

Nelson, R., & Papaloizou, J. C. B. 2002b, MNRAS, in press

Nelson R., Papaloizou, J., Masset, F., & Kley, W. 2000, MNRAS, 318, 18

Shakura, N. I., & Sunyaev, R. A. 1973, A&A, 24, 337

Steinacker, A., & Papaloizou, J. C. B. 2002, ApJ, 571, 413

Stone, J. M., & Balbus, S. A. 1996, ApJ, 464, 364

Stone, J. M., & Norman, M. L. 1992a, ApJS, 80, 753

Stone, J. M., & Norman, M. L. 1992b, ApJS, 80, 791

Takeuchi, T., Miyama, S. M., & Lin, D. N. C. 1996, ApJ, 460, 832

Tanaka, H., Takeuchi, T., & Ward, W. R. 2002, ApJ, 565, 1257

Ward, W. R. 1986, Icarus, 67, 164

Ward, W. R. 1997, Icarus, 126, 261

This figure "f1.jpg" is available in "jpg" format from:

<http://arxiv.org/ps/astro-ph/0301589v1>

This figure "f6.jpg" is available in "jpg" format from:

<http://arxiv.org/ps/astro-ph/0301589v1>

This figure "f11.jpg" is available in "jpg" format from:

<http://arxiv.org/ps/astro-ph/0301589v1>